ARCHIVIO ISTITUZIONALE
DELLA RICERCA

Alma Mater Studiorum Università di Bologna
Archivio istituzionale della ricerca

Wavefield analysis tools for wavenumber and velocities extraction in polar coordinates

This is the final peer-reviewed author's accepted manuscript (postprint) of the following publication:

Published Version:
Malatesta M.M., Moll J., Kudela P., Radzienski M., De Marchi L. (2022). Wavefield analysis tools for wavenumber and velocities extraction in polar coordinates. IEEE TRANSACTIONS ON ULTRASONICS FERROELECTRICS AND FREQUENCY CONTROL, 69(1), 399-410 [10.1109/TUFFC.2021.3106040].

Availability:
This version is available at: https://hdl.handle.net/11585/843951 since: 2022-01-04

Published:
DOI: http://doi.org/10.1109/TUFFC.2021.3106040

Terms of use:

Some rights reserved. The terms and conditions for the reuse of this version of the manuscript are specified in the publishing policy. For all terms of use and more information see the publisher's website.

This item was downloaded from IRIS Università di Bologna (https://cris.unibo.it/).
When citing, please refer to the published version.

(Article begins on next page)

13 November 2026

This is the final peer-reviewed accepted manuscript of:

M. M. Malatesta, J. Moll, P. Kudela, M. Radzieński and L. De Marchi, "Wavefield Analysis Tools for Wavenumber and Velocities Extraction in Polar Coordinates," in *IEEE Transactions on Ultrasonics, Ferroelectrics, and Frequency Control*, vol. 69, no. 1, pp. 399-410, Jan. 2022

The final published version is available online at:

https://doi.org/10.1109/TUFFC.2021.3106040

Terms of use:

Some rights reserved. The terms and conditions for the reuse of this version of the manuscript are specified in the publishing policy. For all terms of use and more information see the publisher's website.

This item was downloaded from IRIS Università di Bologna (https://cris.unibo.it/)

When citing, please refer to the published version.

Wavefield analysis tools for wavenumber and velocities extraction in polar coordinates

Michelangelo Maria Malatesta, *Student Member, IEEE,* Jochen Moll, *Member, IEEE,* Pawel Kudela, Maciej Radzienski, and Luca De Marchi, *Member, IEEE*

***Abstract*—Experimental characterization of Lamb waves in plate–like structures overcomes the intrinsic limits of *a–priori* Semi–Analytical Finite Elements simulations, where material inaccuracies and non–idealities can not be easily considered. Unfortunately, the experimental extraction of guided waves dispersion curves, and especially their polar representation along different directions of propagation at a given frequency, is not trivial. In non-isotropic materials, such analysis is a key aspect for a reliable and robust characterization of the waves behaviour. In this work, by exploiting Scanning Laser Doppler Vibrometer measurements with narrowband excitation, two different signal processing methods for the extraction of the wavenumber polar representation at the excitation frequency are investigated and characterized. The first method is based on a Distance Regularized Level Set algorithm, widely used in image processing and computer vision but, to the best of author's knowledge, never used in the Lamb waves' field. The second method is based on the two-dimensional sparse wavenumber analysis which exploits the wavefield sparse representation in the wavenumber domain. With a precise and reliable extraction of the wavenumber characteristic in the *k*–space, the polar representations at the excitation frequency of phase and group velocities can be estimated. The former, by exploiting the well-known wavenumber–frequency relation, the latter, instead, by computing numerical derivative among wavenumbers at multiple frequencies. The methodology has been validated on three different composite plates with different degrees of non-isotropy properties. The results show the effectiveness of the two methods, highlighting the advantages and disadvantages of both.**

***Index Terms*—Wavefield Analysis, group velocity, phase velocity, DRLSE, Compressive Sensing, Orthogonal Matching Pursuit.**

I. Introduction

LAMB waves have been extensively exploited among years in the Non-Destructive Evaluation (NDE) and Structure Health Monitoring (SHM) fields due to their low attenuation along big distances and the capability to detect internal or surface damages in thin structures [1]. On the other hand, Lamb waves feature a multimodal and dispersive behavior, which has to be precisely and fully characterized to perform a reliable inspection. The waves propagation and their dispersion curves can be modelled by Finite Element Methods (FEM) [2] or Semi-Analytical Finite Element (SAFE) [3], [4] formulations, such as boundary elements [5], [6], spectral elements [7], transfer matrix methods [8] and global matrix methods [9]. Undoubtedly, the state of the art of modelling tools allow researchers to approach the complexity of Lamb waves propagation and characterize, under certain approximations, the waves behaviour. Limitations occur when the material properties are partially or not known and modelling tools can not be exploited. Moreover, inaccuracies in the elastic constants estimation [10], or slight deviations of the material properties from their nominal values, such as those due to non-homogeneity, may affect the precision and reliability of the simulation. Thus, experimental characterization of the structure under investigation is fundamental to support and integrate the preliminary analysis carried on with modelling tools.

Lamb waves dispersion curves are usually represented in the frequency–wavenumber domain, or as phase and group velocity profiles along specific waves propagation directions. In isotropic materials, the extraction of the dispersion curves along any direction fully characterizes the entire structure, which enables velocity tuning or dispersion compensation [11]–[13]. In literature, many experimental techniques have been presented for dispersion curves extraction. Chang and Yuan [14], as well as Schopfer et al. [15] exploited the Matrix Pencil Method for ridge detection in the wavenumber domain to extract dispersion curves from Laser Doppler Vibrometer (LDV) measurements. Harb and Yuan [16], by exploiting an air-coupled transducer as actuator with a specific angle of incidence and a LDV, were able to compute the dispersion curves by means of Snell laws. In [17], the same result was achieved by measuring the phase difference and time lag between two pulses acquired by two different transducers, placed at different distances from the actuator. Conversely, in anisotropic materials, the dependence of the dispersion curves with respect to the direction - or angle - of propagation must be considered. This can be done by repeatedly extracting the dispersion curves along multiple directions [18]–[20]. Moreover, time–frequency based methods effectiveness may be compromised when the inspected structures are characterized by complex geometries and multi–path interference. Unfortunately, in literature, there are very few examples regarding efficient methods for the experimental extraction of dispersion curves along with multiple directions of propagation simultaneously. In [21], an extension of the conventional 2D analysis in the *f-k* domain to 3D *f-*k_x*-*k_y domain is presented. For a given frequency, the wavenumber characteristic along different directions for different propagation modes is revealed in the k_x-k_y domain, a.k.a. *k*–space or 2D wavenumber domain. Moreover, the results show the possibility to perform many signal processing techniques, such as Lamb waves decomposition, mode filtering or short–space Fourier transform. However, the extraction of the wavenumber polar representation in the 2D wavenumber domain is not addressed. In general, this is a not trivial task, since the commonly used time–frequency ridge detection

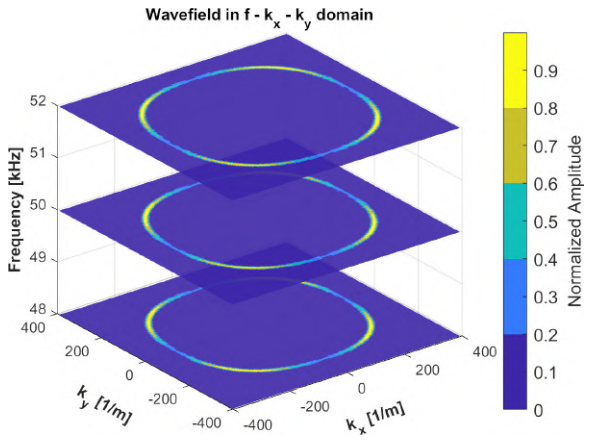

Fig. 1: Wavefield representation in the 3D Fourier Domain.

techniques [22] can not be applied to circle or elliptical shapes. Sabeti et al. [23], instead, presented a comparative study on compressing sensing techniques for full wavefield reconstruction from a subsampled dataset by exploiting the sparsity of the frequency–wavenumber representation. Since the wavefield reconstruction is based on the dispersion curves computation the method implicitly estimates the wavenumber curves. In particular, two techniques suitable for anisotropic plates were addressed, namely the Anisotropic Sparse Wavefield Analysis (ASWA) and the two–Dimensional Sparse Wavefield Analysis (2DSWA). ASWA can achieve very high levels of compression, but can not handle edge or scatters reflections. Moreover, it generally reconstructs only the dominant wavefield mode. Conversely, 2DSWA cannot achieve a very high level of compression, but it is theoretically suitable to reconstruct reflections and multi–mode propagation. However, in [23], the accuracy of this method in wavenumber extraction was not characterized.

In this context, the objective of this work is twofold:

- A new robust approach to extract dispersion curves from wavefield data is introduced. The approach is based on the Distance Regularized Level Set (DRLSE) algorithm [24] applied to the 3D Fourier transform of full wavefield acquisitions. The DRLSE approach has been previously exploited in bio–medical applications [25], [26], materials characterization [27] and radar [28], but was never applied to wavefield analysis.
- Then, the DRLSE method is exploited to characterize the performance and limitations of the 2DSWA on multiple wavefield datasets acquired with Scanning Laser Doppler Vibrometers (SLDVs) and, in particular, the trade–off between compression capabilities and accuracy of dispersion curves reconstruction is explored.

II. Theoretical Background

A. Wavenumber polar representations

A SLDV can measure the Lamb waves wavefield in time and space over a defined scanning area with high spatial resolution and high signal–to–noise ratio. Therefore, it is a very attractive technology for Lamb waves characterization and monitoring [29]. In particular, by exploiting the *frequency–wavenumber* representation of the acquired wavefield, computed by a 2D–Fourier Transform (2DFT), it is possible to extract useful information related to both the wavenumber as a function of the frequency and the multimodal propagation of the waves [30]. By exploiting a 3D–Fourier Trasform (3DFT), instead, the wavefield in the $f-k_x-k_y$ domain or 3D Fourier domain can be computed, as depicted in Fig. 1. Each slice at a given frequency is addressed as *k*–space or 2D wavenumber domain wavefield representation. Many signal processing techniques in the 3D Fourier domain have been developed, such as mode separation [31], wavenumber filtering [32] and wavefield manipulation [33]. Multiscale representations such as those generated by multidimensional Wavelet [34] or Curvelet transforms [35] allow to better track non-stationary effects. It is worthy to notice that usually, a 2D spatial filtering is performed before running the 3DFT in order to reduce the border effects which may lead to artefacts in the transformation domain [36]. For instance, a Gaussian window can be used [37]. Nevertheless, the extraction of the wavenumber profile for a fixed f_i is not trivial, due to the closed–loop shape which inhibits the exploitation of conventional ridge detection algorithms. Recently, Ma and Yu [38] presented a maximum–tracking based technique, in which, after the conversion from the Cartesian $U(f_i, \mathbf{k})$ to the polar $U(f_i, r, \theta)$ plane, for each angle θ the radius at the maximum wavenumber index value was extracted. The drawback of this method is the high sensitivity to noise.

B. The Distance Regularized Level Set method

In this work, we propose to exploit the Distance Regularized Level Set (DRLSE) algorithm [24] to analyze wavefield data. The main advantage of Level Set (LS) algorithms for image processing is their capability to extract contours of highly–complex images without any parametrization. The method is based on the representation of a closed curve as the zero level set of an auxiliary function ϕ called Level Set Function (LSF). Then, iteratively, starting from an initial LSF defined as a binary step function of arbitrary shape, the motion of the closed curve is developed as the evolution of the LSF. When compared with conventional level set approaches, the DRLSE has the advantage that does not require any re–initialization to solve the irregularities of the LSF.

From a mathematical point of view, LSF is defined as $\phi : \Omega \rightarrow \Re$ term. The level set evolution is derived as a gradient flow that minimizes an energy functional $\mathcal{E}(\phi)$:

$$\mathcal{E}(\phi) = \mu\mathcal{R}_p(\phi) + \lambda\mathcal{L}_g(\phi) + \alpha\mathcal{A}_g(\phi) \tag{1}$$

where $\mathcal{R}_p(\phi)$ is the level set regularization term, $\mathcal{L}_g(\phi)$ and $\mathcal{A}_g(\phi)$ are energy functionals, $\mu > 0$, $\lambda > 0$ and $\alpha \in \Re$ are constant coefficients for $\mathcal{R}_p(\phi)$, $\mathcal{L}_g(\phi)$ and $\mathcal{A}_g(\phi)$ respectively. To clarify, $\mathcal{R}_p(\phi)$ is defined as :

$$\mathcal{R}_p(\phi) = \int_\Omega p(|\nabla\phi|)\, dx \tag{2}$$

where p is a potential function which is defined in order to have two minimum points (double well points) $p(|\nabla\phi|) = 0$

and $p(|\nabla\phi|) = 1$. In such a way, $|\nabla\phi| = 1$ is maintained only to the proximity of the zero level set, while keeping $|\nabla\phi| = 0$ otherwise. This leads to achieve a strong smoothing effect and an accurate computation during the level set evolution. Conversely, the $\mathcal{L}_g(\phi)$ is an energy functional which is minimized when the zero level contour of ϕ is at the actual contour of the target image, meanwhile $\mathcal{A}_g(\phi)$ is an energy functional introduced to speed up the convergence. The DRLSE main goal is to minimize the energy functional defined in (1). A well established method to minimize an energy functional is to find the steady state solution of the gradient flow equation [39]:

$$\frac{\partial\phi}{\partial t} = -\frac{\partial\mathcal{E}(\phi)}{\partial\phi} \tag{3}$$

Once the steady state is found, the contour of the figure is extracted (for a more in–deep mathematical presentation, see [24]).

C. 2DSWA based method

Compressing sensing techniques allow to sub–sample signals below the Nyquist sampling rate without losing information under certain assumptions [40], [41]. In particular, the signal has to feature sparsity, *i.e.* with only a few nonzero coefficients in a transformation domain, and the samples must be acquired randomly. These concepts can be applied to wavefield analysis. In fact, the wavefield representation in the wavenumber domain is sparse and, consequently, it is possible to reconstruct the wavefield on dense regular grid from subsampled measurements. This technique is referred to as Sparse Wavefield Synthesis (SWS) and is gaining attention in the scientific community since it allows to reduce considerably the acquisition time [41], especially when combined with deep learning methods [42].

Thus, let's consider a random sub–sampled wavefield measurements $y \in R^m$:

$$\mathbf{y} = \Phi\mathbf{x} \tag{4}$$

where $\Phi \in R^{m\times n}$ is the measurement matrix and $x \in R^n$ is the full grid wavefield, *i.e.* without any sub–sampling. Since, as assumption, $\mathbf{x}$ has a sparse representation in some model basis $\Psi \in R^{n\times n}$, (4) can be rearranged as:

$$\mathbf{y} = \Phi\Psi\mathbf{s} = \Theta\mathbf{s} \tag{5}$$

where $\mathbf{s}$ is the sparse representation of $\mathbf{x}$ in the *f-k* domain, aka the wavenumber dispersion curves, and Θ is usually addressed as the *dictionary* [23]. The most suitable dictionary is chosen by considering the analytical Lamb waves model. In particular, the ideal Lamb wave propagation model in the frequency domain for isotropic plate can be expressed as [43]:

$$\mathbf{y}(\mathbf{r},\omega) = \sum\sqrt{\frac{1}{k_n(\omega)r}}G_n(\omega)e^{-jk_n(\omega)r} \tag{6}$$

where r is the actuator–receiver distance, ω is the angular frequency, $k_n(\omega)$ the n–th mode wavenumber dispersion curve and $G_n(\omega)$ is the complex wavenumber amplitude. Equation 6 can be viewed as a linear combination of a set of bases that constitute the wavefield, from which it is possible to define the dictionary Θ as follows:

$$\Theta = \sqrt{\frac{1}{k_n r_m}}e^{-jk_n r_m} \tag{7}$$

Since (5) is an underdetermined system of equations, it can be solved via a sparse recovery algorithm, such as the Orthogonal Matching Pursuit (OMP) technique [44]. Thus, by solving (4) the wavenumber dispersion curves in the $f-k$ domain are extracted.

Since wavefields have a sparse representation even in the $f-k-x-k_y$ domain, as can be noticed in Fig. 1, this approach can be extended in the corresponding 2D problem. This method, referred to as 2DSWA, has been presented by Sabeti and Harley in [23]. In particular, (5) can be rearranged as follows:

$$\mathbf{Y_i} = \Theta_1\mathbf{S_i}\Theta_2^T \tag{8}$$

where $\mathbf{Y_i} \in M_y \times N_x$ is the frequency-domain wavefield at each frequency f_i and $\mathbf{S_i} \in M_y \times M_x$ is the 2–D sparse representation of the wavefield in the $f_i - k_x - k_y$ domain. $\Theta_1 \in M_y \times N_y$ and $\Theta_2 \in M_x \times N_x$, instead, are the left and right dictionaries, which can be defined as spatial Fourier bases that are synthesized with respect to Cartesian coordinates of the grid points and the wavenumber range in each direction:

$$\Theta_1 = e^{-jyk_y^T} \tag{9}$$

$$\Theta_2 = e^{-jxk_x^T} \tag{10}$$

By exploiting 2DSWA model, it is possible to deal with non isotropic Lamb waves propagation. In such a way, the wavenumber polar representation at given frequencies can be extracted enabling the analysis of direction-dependent velocity variations in anisotropic structures [23]. An extensive description of the 2DSWA approach, such as the demonstration of its performance in both isotropic and anisotropic cases, is presented in [45]. To solve (8), a modified 2D version of the OMP algorithm was presented in [46]. As a result, a point cloud for each frequency of interest is extracted in the 2D wavenumber plane. As better discussed in the next section, by applying a fitting procedure the wavenumber polar representation can be estimated. It is worth to notice that this technique is better suited for low undersampling rates, *i.e.* close to the Nyquist rate. On bright side, the usage of 2DSWA does not require additional optimizations and it can handle border reflections and multimodal reconstruction.

III. Materials and Methods

In this work, methodologies based on DLRSE and 2DSWA to extract the wavenumber polar representation from wavefields are presented. From the wavenumber polar representation at multiple frequencies, the phase and group velocity curves can be estimated, enabling a complete experimental wavefield characterization. In particular, three datasets acquired by a SLVD on three Carbon Fiber Reinforced Plates (CFRPs), which feature different anisotropic properties and different acquisition strategies, have been exploited for validation. The first plate, described in [10], presents a slightly

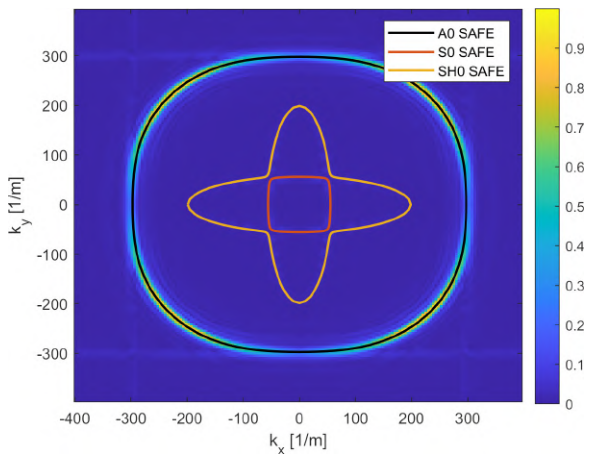

Fig. 2: SANI wavefield in the 2D Wavenumber domain at 50 kHz. SAFE simulations of the A0, S0 and SH0 modes are superimposed.

anisotropic characteristic (SANI dataset). The second one, instead, refers to a unidirectional highly anisotropic plate (HANI dataset). The last dataset (OWG) is related to a plate made of quasi–isotropic laminates and it is freely available (http://www.open-guided-waves.de [47]). Further details are provided below.

A. Experimental setups

The SANI wavefield was acquired on a carbon/epoxy 16–layers laminate. The specimen dimensions are 1200x1200 mm with average thickness 3.9 mm and density $1522.4\,^{kg}/_{m^3}$. On the other hand, the HANI laminate features 40 layers made of unidirectional carbon/epoxy fibers. In this case, the plate dimensions are 1200x1200 mm for 2.85 mm of thickness and density $1574\,^{kg}/_{m^3}$. A piezoelectric PZT disk of 10 mm diameter was attached at the centre of both the CFRP plates. Since the layups of the specimens yield the same propagation characteristics in all four quadrants, just one quarter of the plate was scanned with the SLVD (Polytec PSV-400), with the PZT disk in the upper right corner. The excitation signal was a narrowband signal with a central frequency of 50 kHz. In the previous works of Kudela et al. [10] and [48], the SANI and HANI plates were characterized by broadband measurements. In particular, the theoretical elastic constants of the SANI and HANI laminates were estimated by means of a Genetic Algorithm (GA) which finds the best matching between the numerical model and experimental data. The obtained material parameters, which are shown in TABLE I, have been used in this work for the calculation of theoretical dispersion curves by SAFE simulations, enabling the evaluation of the proposed methods by reliable accuracy metrics.

The last dataset was acquired on a plate made of prepreg material Hexply M21/T700, with dimensions 500x500 mm and 2 mm of thickness. The laminates feature a layup $[45/0/-45/90/-45/0/45/90]_S$ which makes the waves propagation quasi–isotropic. A 5 mm diameter PZT transducer was bounded at the centre of the plate and used as actuator. The wavefield was acquired by a SLVD (Polytec PSV-400) on one

C	SANI	HANI
C_{11}	52.55	138.67
C_{12}	6.51	5.72
C_{13}	5.94	6.53
C_{22}	51.83	12.36
C_{23}	5.88	5.99
C_{33}	10.28	11.80
C_{44}	2.93	3.12
C_{55}	2.92	5.11
C_{66}	3.81	4.89

TABLE I: The optimized elastic constants of the SANI [10] and HANI [48] plates [GPa]

quarter of the plate as acquisition window, with the PZT transducer in the upper right corner. A narrowband 60 kHz wave was used as excitation signal. The measurements were performed at a fixed temperature of 23 °C and averaged 100 times for reducing noise. The wavefield propagation characteristics feature a central symmetry, i.e. $u(r,\alpha) = u(r,\alpha+\pi)$, where $u(r,\alpha)$ is the wavefield in polar coordinates. Thus, to fully characterize the dispersion curves in their polar representation, the wavenumber must be extracted in a 180° range. Since one quarter of the plate was scanned, the direct propagation was fully characterized just in 90° range. Information along with the remaining 90° was extracted by a signal processing procedure which isolates the reflections from the plate edges with a time filtering. Then, the filtered wavefield in the 2D wavenumber domain is normalized and processed to enhance the reflections contribution. An in–depth description of the signal processing procedure is presented in the next section.

Finally, it's worthy to mention that the proposed signal processing can be applied to narrowband or broadband measurements at any excitation frequency, taking into account that SLDV has good, quite uniform sensitivity in the range up to about 300kHz. Above that frequency, signal amplitudes are weak due to material damping, noise and SLDV limited abilities. Moreover, at lower frequencies, only A0, S0 and SH0 modes propagate which can be captured by the SLDV. In particular, SLDV measures particle velocities perpendicular to the surface of the specimen, which are dominant in A0 mode. For this reason, only the extraction of the antisymmetric mode A0 will be addressed.

1) Fourier–DRLSE approach: The main steps of the Fourier–DRLSE processing are shown in Fig. 3. At first, time windowing is applied to cancel out noise and undesired edge reflections from the wavefield. In particular, a 500 µs time window was used in the case of SANI and HANI datasets, while a 600 µs window was exploited in the OGW case. Moreover, a spatial 2D Gaussian filtering defined as:

$$G(x,y) = \frac{1}{2\pi\sigma^2} e^{-\frac{x^2+y^2}{2\sigma^2}}$$

with standard deviation $\sigma = 0.5$, has been implemented to mitigate border artefacts. Then, the amplitude of the 3DFT coefficients is normalized in the interval [0,1]. In Fig. 4a, the SANI Wavefield in the 2D wavenumber domain at the fundamental frequency of 50 kHz is shown. As expected, the main energetic contribution shapes the wavenumber characteristic clearly in only one quadrant, *i.e.* along 90° of propagation. By mirroring the obtained profile, it is possible to reconstruct

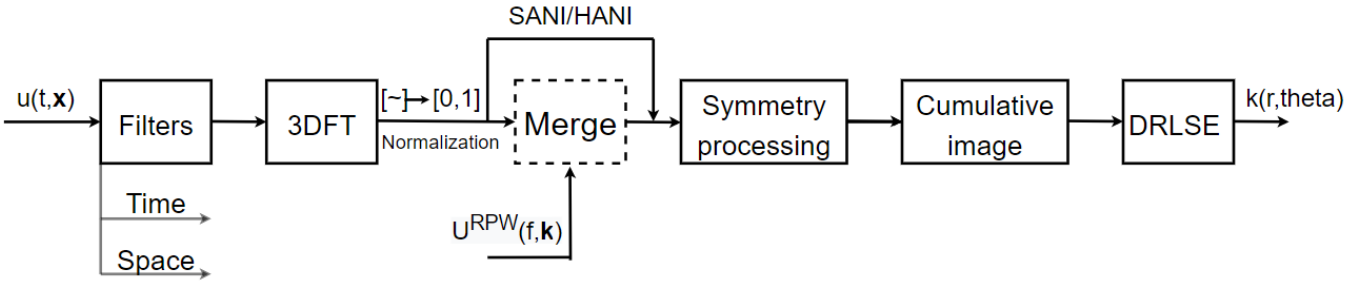

Fig. 3: DRLSE–based signal processing. $U^{RPW}(f, \mathbf{k})$ is the OGW Reflected Paths Wavefield in the Fourier domain

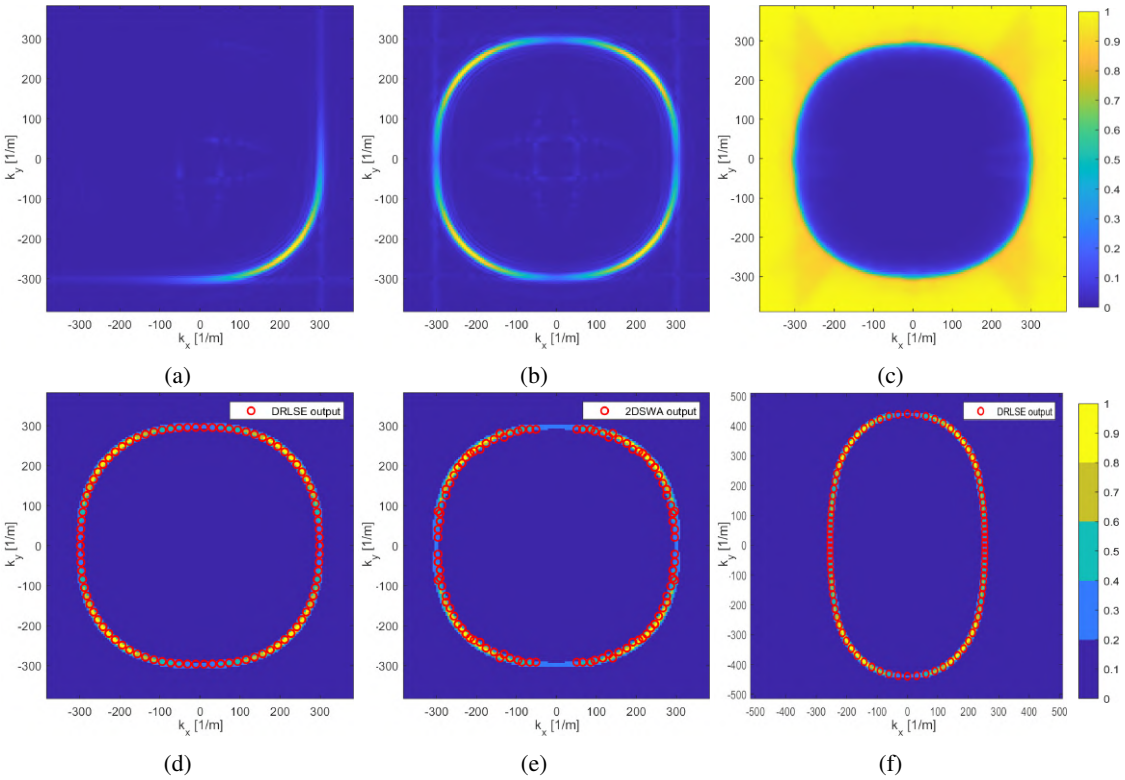

Fig. 4: SANI and HANI wavenumber extraction: (a) SANI 3DFT output at 50 kHz. (b) SANI wavefield in the 2D wavenumber domain after the 'symmetry processing'. (c) SANI cumulative image, (d,e) SANI DRLSE, 2DSWA output. (f) HANI DRLSE output. The colorbars on the right refer to the plots of the same row.

the characteristic along all the 360° of propagation. Similar results are achieved with HANI data. Conversely, in the OGW case without any reflection filtering, shown in Fig. 5a, the wavenumber profile in the *k*–space is sufficiently energetic just in one quadrant. Information of reflections in the other quadrants present a very low signal–to–noise ratio. Furthermore, because of the strong attenuation of the multiple reflection paths, the wavenumber profile is not visible in some propagation directions. To tackle these limitations, the acquired wavefield was divided into two subsets related to distinct time intervals, i.e. $[0 - 400\,\mu s]$ and $[200\,\mu s - 600\,\mu s]$. In the first interval, the direct wave was dominant, while the second interval was mostly characterized by the presence of edge reflections. An overlap between the two time windows was used to reduce artifacts and maximize the wavefield energy. The two subsets were processed with the previously described steps. After the normalization step, the processing results of the two branches are merged by selecting for each element of the two matrices the highest intensity value. Then, processing which exploits the symmetry of the waves propagation is performed. In the SANI and HANI cases, the wavenumber profile has been mirrored in all the quadrants. In the OGW dataset, instead, the central symmetry property $U(r, \alpha) = U(r, \alpha + \pi)$ has been exploited. The result in the SANI case is depicted in Fig. 4b. As can be observed, the A0, S0 and SH0 modes profiles exist, even if the A0 mode features higher intensity. In Fig.2, theoretical dispersion curves are superimposed to the processed wavefield in the 2D wavenumber domain. Since the DRLSE is able to reconstruct a single closed loop shape, only one mode can be processed. Thus, a 2D wavenumber filter is

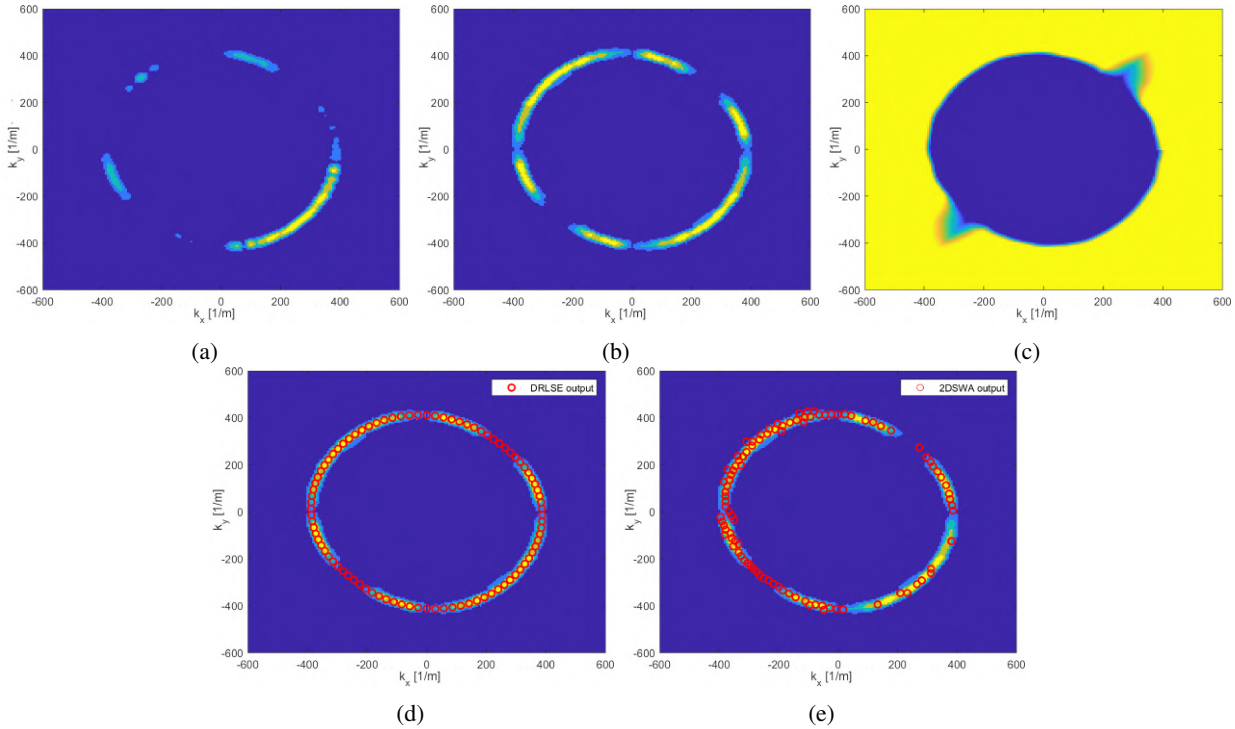

Fig. 5: OGW wavenumber extraction: (a) 3DFT output at $60\,\mathrm{kHz}$ without any pre–processing. (b) $U(f_{60\,\mathrm{kHz}}, \mathbf{k})$ after the 'merge' processing block. (c) Cumulative image. (d,e) DRLSE,2DSWA wavenumber extraction

applied. In this work, S0 and SH0 modes were filtered out to address the extraction of the A0 wavenumber profile. Anyway, the procedure can be theoretically carried on similarly to any propagation mode. Before applying the DRLSE algorithm, a further pre–processing block is necessary. Indeed, the DRLSE is essentially an edge detection algorithm, therefore, to generate artificial edges we have processed the magnitude of the Fourier coefficients by computing the cumulative function of $U(f_i, k_x, k_y)$ along each propagation angle. Then, the cumulative functions are interpolated in a cartesian grid. The image amplitude is normalized and a contrast enhancement filter is applied to further help a fast and reliable convergence of the DRLSE algorithm. Examples of generated *cumulative images* are depicted in Fig. 4c and Fig. 5c, for the SANI and OGW cases. Finally, the DRLSE algorithm is applied to the processed image and the wavenumber profile along all the directions of propagation is obtained. In Fig. 4d, the SANI final wavenumber reconstruction, superimposed to the corresponding wavefield Fourier transform, is shown, revealing an almost perfect overlap. Similar good results were achieved with the OGW (see Fig. 5d) and HANI datasets (Fig. 4f). It is worth noting that the DRLSE algorithm is able to reconstruct correctly the entire wavenumber profile even if the information in some angular ranges is very weak. This is a distinctive feature of the DRLSE method and shows its robustness and reliability in a very complicated application case. In fact, the flexibility in the wavefield pre–processing, which can be customized easily with respect to the specific scenario, allows optimizing the DRLSE convergence even in datasets with low signal–to–noise ratios.

2) 2DSWA based approach: In the 2DSWA based approach, the pre–processing consists in: i) a time windowing to reduce the reflections; ii) a band pass filtering for signal denoising. In particular, since the fundamental excitation frequency of the SANI and HANI wavefields is $50\,\mathrm{kHz}$, the spectral content from $42\,\mathrm{kHz}$ to $58\,\mathrm{kHz}$ was considered in this case. Conversely, frequencies from $50\,\mathrm{kHz}$ to $70\,\mathrm{kHz}$ have been used in the OGW case. This pre-processing is followed by the actual compressive sensing. In particular, a random sampling strategy with sub–sampling ratio $R_{UN} = 34.9\,\%$, $R_{UN} = 34.96\,\%$ and $R_{UN} = 83.3\,\%$ have been chosen for the SANI, HANI and OGW datasets, respectively. R_{UN} has been computed as follows:

$$R_{UN} = \frac{N_U}{N_{Nyq}} \tag{11}$$

where N_U is the number of points on the random sample grid and N_{Nyq} is the number of the points in the Nyquist grid [23]. The 2DSWA method is then applied and the sparse representation of the wavefield is obtained. The 2DSWA output of the SANI dataset and its accordance with the corresponding wavefield Fourier transform at $50\,\mathrm{kHz}$, is depicted in Fig. 4e. In Fig. 5e, the 2DSWA output at $60\,\mathrm{kHz}$ and the corresponding Fourier representation of the OGW wavefield in the *k*–space is shown. Since the 2DSWA output is a point cloud, a fitting procedure based on Fourier series is exploited to determine the wavenumber profile [49], after a mode filtering, if required. Finally, the wavenumber polar representation is extracted. It is qualitatively evident, looking at Fig. 4e and Fig. 5e, that the 2DSWA approach provides a good tracking of wavenumber profile. In the next section, a more detailed analysis will

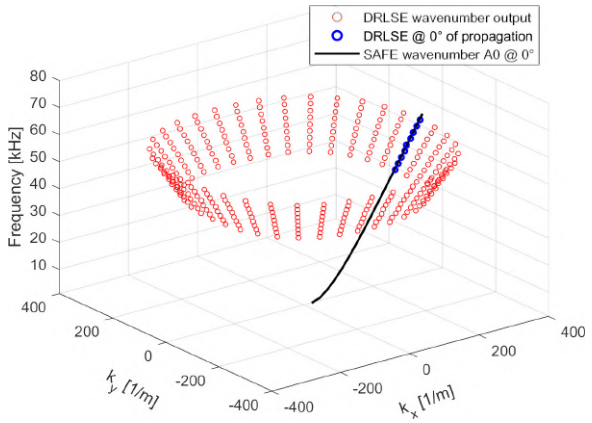

Fig. 6: Single–mode A0 wavenumber reconstruction for frequencies from $42\,\mathrm{kHz}$ to $58\,\mathrm{kHz}$ with a step of $2\,\mathrm{kHz}$ by DRLSE method. In black the theoretical A0 wavenumber along with 0° direction of propagation by SAFE simulation.

$R_{UN}[\%]$	Max$[m^{-}1]$	Average $[m^{-}1]$
83.3	4.72	2.79
41.66	5.47	3.15
31.26	6.63	2.37
23.45	76.46	32.17

TABLE II: OGW wavenumber reconstruction errors by 2DSWA method varying R_{UN}

be carried out to investigate the algorithm performance for different subsampling ratios.

IV. Results

A. Wavenumber extraction characterization

To evaluate the precision of the proposed methods, SAFE simulations were used as reference for SANI and HANI datasets. In particular, in Fig. 7a, 7b, 7d, and 7e, the final DRLSE and 2DSWA outputs are superimposed to the SAFE simulations. In both cases, the fundamental excitation frequency of $50\,\mathrm{kHz}$ was considered. In Fig. 7c and 7f, the DRLSE and 2DSWA errors at each propagation angle are plotted for the SANI and HANI datasets, respectively. It can be observed that the DRLSE results match extremely well the simulations. The 2DSWA approach shows a lower precision, but the wavenumber reconstruction is still satisfactory if we take into account that a sub–sampling of about $R_{UN} = 35\,\%$ was performed. In Fig. 7g the error characterization of the SANI wavenumber, extracted at compression rates $R_{UN} = 34.9\,\%$, $R_{UN} = 17.43\,\%$ and $4.36\,\%$, is depicted. As can be seen, the error rises by reducing R_{UN}, especially in the local maxima. Anyways, it remains below $8\,\mathrm{m}^{-1}$, even with a compression rate of $4.36\,\%$. This means that a sufficiently accurate wavenumber reconstruction is possible with significant compression levels. In Fig. 7h, the same analysis is carried on for the HANI dataset. Similarly to the previous case, the errors oscillate below $8\,\mathrm{m}^{-1}$. Therefore, the same conclusions can be drawn.

In the OGW dataset, since the elastic constants optimized by GA were not available, SAFE simulations could not be considered as a reliable reference. Thus, we relied on the DRLSE outputs to characterize those achieved with 2DSWA. This is due to the fact that the DRLSE OGW wavenumber profile is perfectly superimposed to the wavefield in the Fourier domain, as it can be observed in Fig. 5d. In Fig. 7i, 7j and 7k, the wavenumber reconstruction among different compression rates is depicted. In TABLE II the maximum and average errors at each compression rate are shown. The performances at $R_{UN} = 83.3\,\%$, $R_{UN} = 41.66\,\%$ and $R_{UN} = 31.26\,\%$ are comparable, while the error rises dramatically at lower R_{UN}, such as $R_{UN} = 23.45\,\%$. It is worthy to notice that the compression rates are significantly higher w.r.t. the other datasets to achieve a good estimation.

B. Phase and group velocity extraction

Once a precise wavenumber estimation is performed, the phase and group velocity can be computed. The first quantity is computed by exploiting the simple wavenumber–phase velocity relationship:

$$v_p(r,\theta) = \frac{\omega}{k(r,\theta)} \tag{12}$$

where ω is the angular frequency. Conversely, the group velocity estimation is not trivial, since a derivative operation is involved:

$$v_g(r,\theta) = \frac{\partial \omega}{\partial k} \tag{13}$$

In literature, the derivative is usually computed numerically only in propagation models, where the wavenumber behaviour among frequencies can be estimated very precisely [50]. Thanks to the high precision wavenumber reconstructions obtained in this work, we propose to exploit numerical derivative even with experimental data. In particular, in the case of the SANI and HANI wavefields, the wavenumber $\mathcal{W}(f,r,\theta)$ has been extracted for frequencies from $42\,\mathrm{kHz}$ to $58\,\mathrm{kHz}$, with a step of $\Delta f = 2\,\mathrm{kHz}$. In Fig.6, for instance, the A0 wavenumber profiles extracted by means of DRLSE in (k_x, k_y) coordinates are shown. The blue dots are the wavenumbers values along with the 0° direction, superimposed with the theoretical dispersion curve in black. Then, the $\mathcal{W}(r,f)|_{\theta=\theta_i}$ profile, at each fixed propagation angle has been interpolated by a second–order polynomial method, reducing the frequency step to $100\,\mathrm{Hz}$. Finally, the numerical derivative was computed. In particular, the chosen derivation strategy is based on calculating the central difference for interior data points. Meanwhile, single-sided differences are computed along the edges of the numerical vector. The procedure is then repeated for each propagation direction. In Fig. 8, instead, the computed phase and group velocities are shown. The estimation of the wavenumbers was carried on by the DRLSE and 2DSWA approaches. In the 2DSWA computations, compression rates of $R_{UN} = 34.9\,\%$ and $R_{UN} = 34.96\,\%$ were used as references for the SANI and HANI plates, respectively. The maximum and average errors of the velocities w.r.t. SAFE simulations are shown in TABLE III. The performance of the DRLSE approach is slightly better in comparison with the 2DSWA in both the SANI and HANI datasets, as expected. Anyway, the 2DSWA method was able to reconstruct the dispersion curves

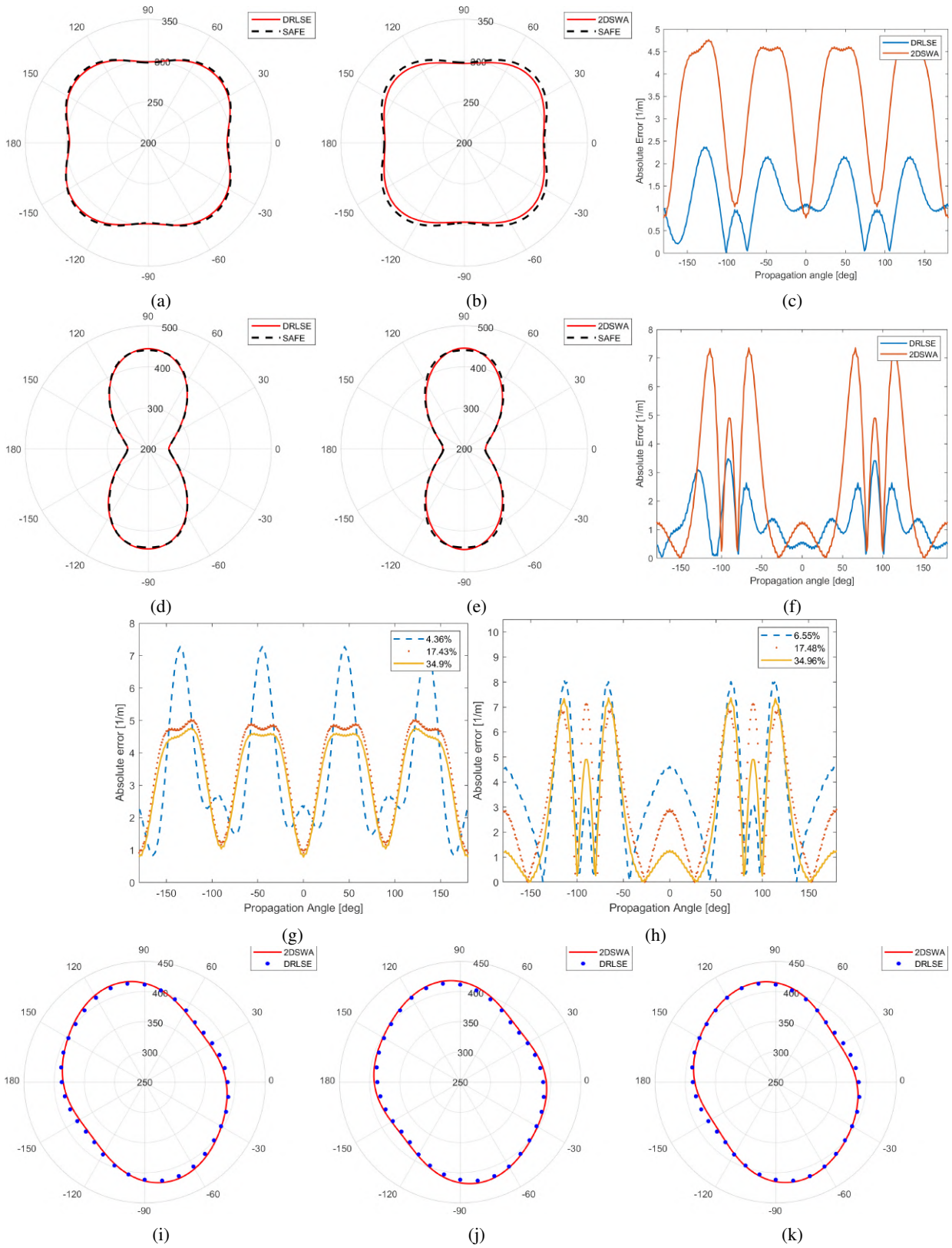

Fig. 7: Wavenumbers extraction results ($[\mathrm{m}^{-1}]$): (a,d) SANI,HANI DRLSE wavenumber reconstruction compared with SAFE simulation. (b,e) SANI,HANI 2DSWA wavenumber recontruction compared with SAFE simulation. (c,f) SANI,HANI error comparison between the two methods. (g,h) 2DSWA error analysis varying R_{UN} for the SANI,HANI datasets. (i,j,k) 2DSWA wavenumber reconstruction for the OGW dataset with $R_{UN} = 83\%, 41\%, 31\%$, respectively, compared with DRLSE output.

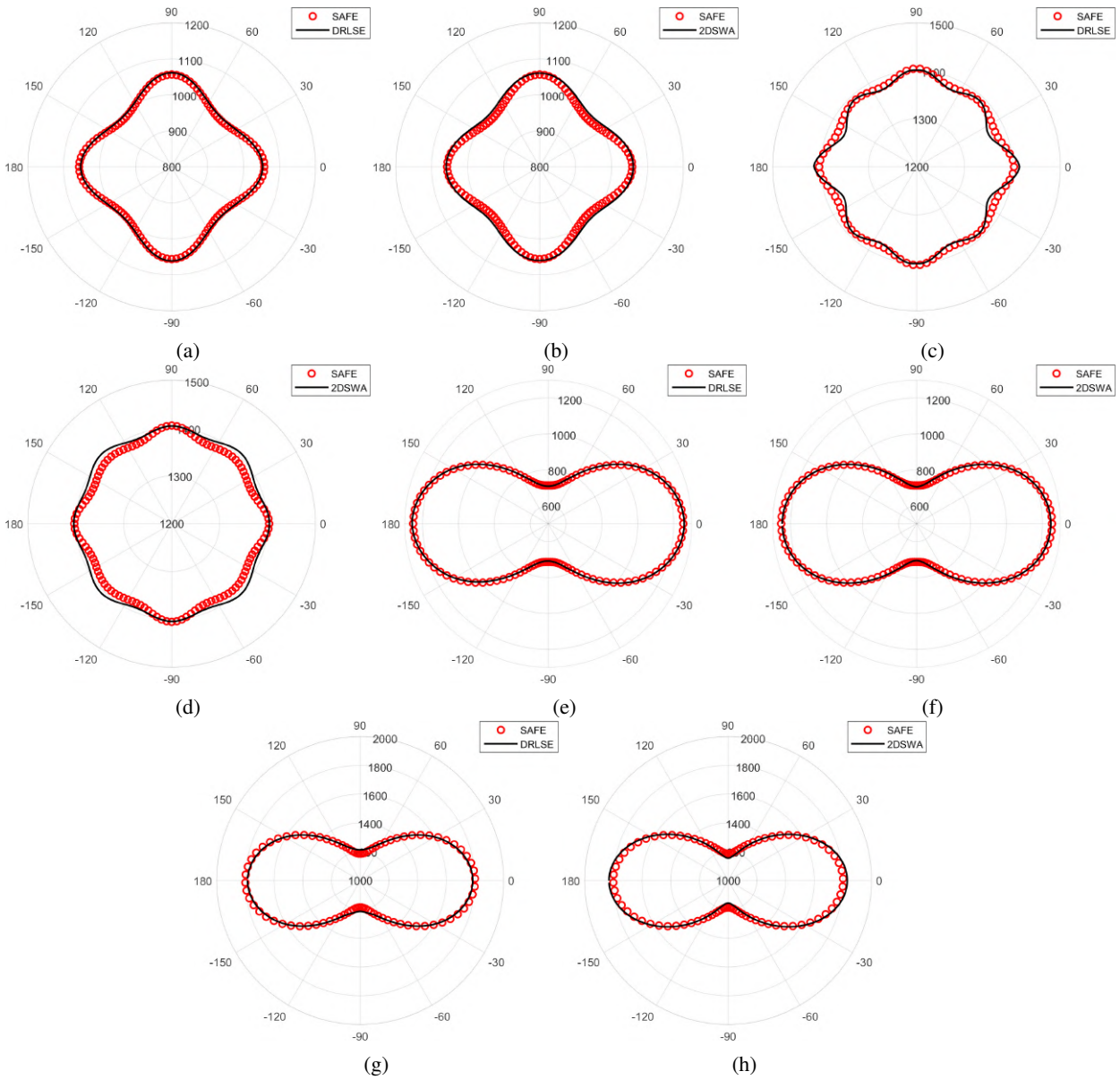

Fig. 8: Phase and group velocity results ([m/s]) for SANI and HANI datasets. In particular: (a,b) SANI v_p by DRLSE,2DSWA methods. (c,d) SANI v_g by DRLSE,2DSWA methods. (e,f) HANI v_p by DRLSE,2DSWA methods. (g,h) HANI v_g by DRLSE,2DSWA methods.

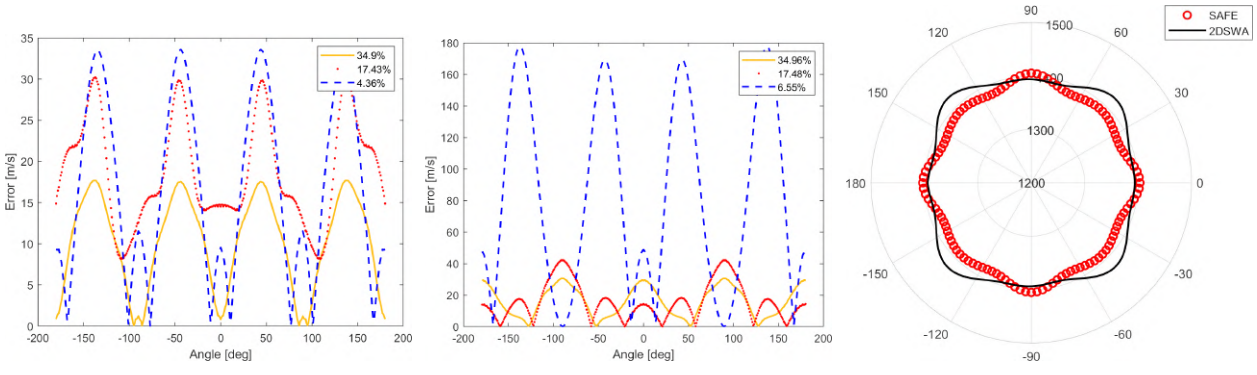

Fig. 9: (a,b) v_g error characterization at different R_{UN} for SANI,HANI datasets. (c) SANI v_g at $R_{UN} = 4.36\,\%$

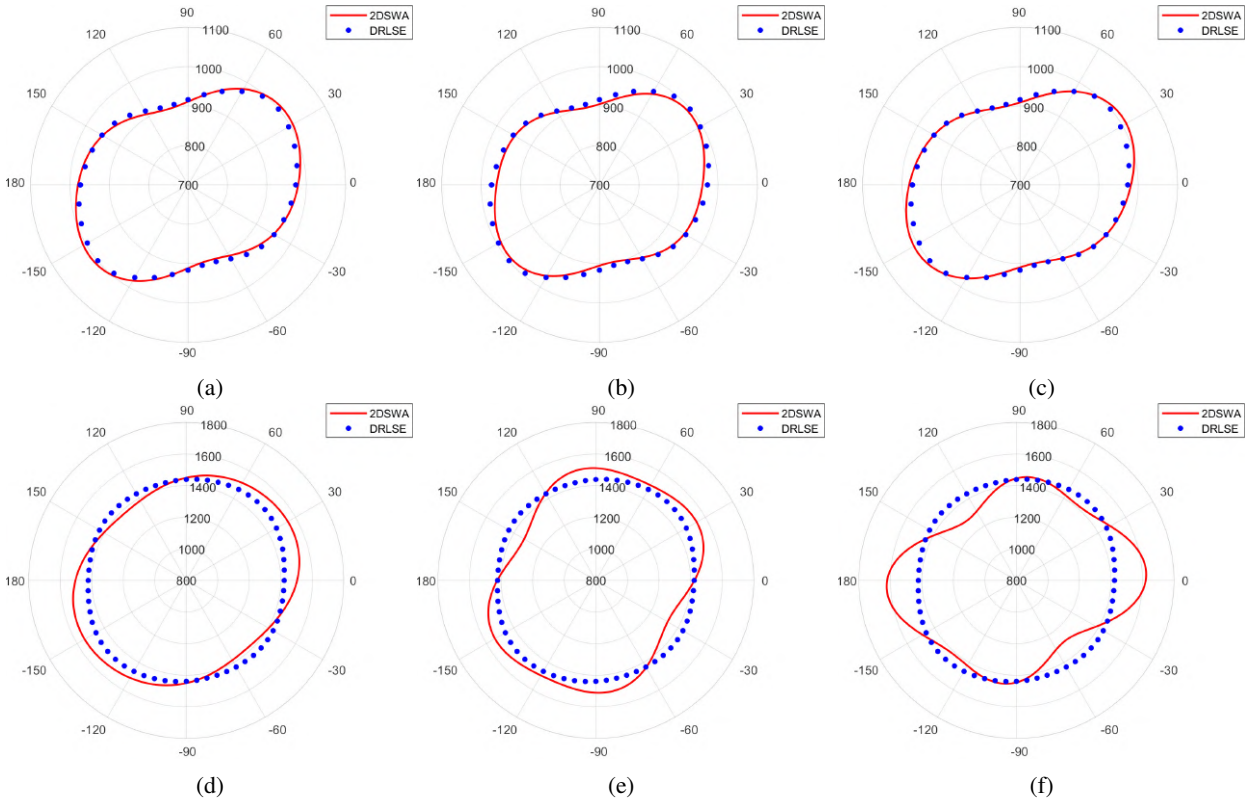

Fig. 10: OGW dataset phase and group velocity results ([m/s]): (a,b,c) v_p at $R_{UN} = 83.28\,\%$, $R_{UN} = 41.66\,\%$, $R_{UN} = 31.26\,\%$. (d,e,f) v_g at $R_{UN} = 83.28\,\%$, $R_{UN} = 41.66\,\%$, $R_{UN} = 31.26\,\%$

	Max[m/s]	Average [m/s]
SANI DRLSE v_p	7.48	3.84
SANI 2DSWA v_p	15.31	10.9
HANI DRLSE v_p	8.01	3.36
HANI 2DSWA v_p	14.38	5.91
OGW 2DSWA v_p	12.5	6.79
SANI DRLSE v_g	14.74	5.35
SANI 2DSWA v_g	17.71	10.16
HANI DRLSE v_g	29.04	11.62
HANI 2DSWA v_g	30.6	16.05
OGW 2DSWA v_g	113.53	66.93

TABLE III: Phase and group velocity errors. In the 2DSWA cases, R_{UN} at $34.9\,\%$, $34.96\,\%$ and $83.3\,\%$ were considered for the SANI, HANI and OGW datasets, respectively

very closely with respect to the DRLSE, with a compression rate of about $35\,\%$. Thus, the group velocity estimation with different compression rates has been investigated to determine the minimum R_{UN} achievable. In Fig. 9 the errors of the group velocity estimations for the SANI and HANI datasets at different R_{UN} are depicted. As expected, by reducing R_{UN} the quality of the group velocities gets worse. In particular, the SANI group velocity reconstruction can be considered successful only for $R_{UN} = 34.95\,\%$ and $R_{UN} = 17.43\,\%$. In fact, even if the errors in absolute terms remain below $35\,m/s$ at a compression rate of $4.36\,\%$, the velocity shape in polar coordinates is not satisfactory and do not follows anymore the expected profile (Fig. 9c). Similarly, the HANI group velocity is satisfactory at $R_{UN} = 34.9\,\%$ and $R_{UN} = 17.48\,\%$. The error rises dramatically at $R_{UN} = 6.55\,\%$, instead.

Finally, the OGW velocity curves analysis is addressed. $\mathcal{W}(f, r, \theta)$ has been extracted for frequencies from $50\,\text{kHz}$ to $70\,\text{kHz}$, with a step of $\Delta f = 2.5\,\text{kHz}$, and then interpolated. To facilitate the group velocity estimation, the interpolation frequency step was reduced to $\Delta f = 10\,\text{Hz}$. In Fig. 10 the phase and group velocities are depicted with $R_{UN} = 83.3\,\%$, $R_{UN} = 41.66\,\%$ and $R_{UN} = 31.26\,\%$, from left to right, respectively. Nevertheless, the obtained group velocity errors are not negligible, with a maximum of $113.53\,m/s$ and average $66.93\,m/s$ at $R_{UN} = 83.3\,\%$. In the other cases, the errors are even higher and, as it can be observed in Fig. 10e and 10f, the extracted profiles are distorted and do not follow anymore the expected behaviour. Thus, it is evident that the 2DSWA approach was not able to properly reconstruct the group velocity in this application case. On the other hand, the phase velocity computation shows good accordance in all the compression rates shown.

V. Conclusion

In this work, the wavenumber, phase and group velocities for the A0 mode in polar coordinates at a given frequency have been extracted experimentally from narrowband SLDV wavefield measurements. In particular, the performance and capabilities of two different methods have been investigated. The first approach relies on the extraction of the wavenumber profile in the *k*–space obtained by 3DFT and proper signal pre–processing. A DRLSE algorithm has been used to precisely determine the closed–loop ridge in the Fourier domain at a

fixed frequency. The second approach, namely the 2DSWA, is based on subsampling the wavefield in the frequency–space domain in order to extract the Wavenumber profile by a two dimensional OMP strategy which exploits the inherent signal sparsity. From the obtained frequency–wavenumber dependencies, phase and group velocities were extracted. The presented results showed how the DRLSE approach was able to reliably reconstruct the dispersion curves in all the proposed application cases. The 2DSWA showed very close performances to the DRLSE approach in the SANI and HANI datasets, achieving high compression levels. In such cases, the compressive sensing strategy is very effective since sub–sampling in the measurement stage might be exploited for speeding up the SLDV acquisitions. On the contrary, in the OGW dataset, which is characterized by high complexity and low signal–to–noise ratio, the performances of the 2DSWA are much poorer. From this analysis, it can be concluded that the DRLSE method is a robust and reliable technique for the wavenumber and velocities extraction in polar coordinates at a given frequency thanks to its flexibility in the signal pre/post processing which can be customized to the experimental data of interest. While the 2DSWA is a viable alternative in high signal–to–noise ratio measurements to speed up the characterization of materials. As future developments, it's worthy to mention the possibility to further extend the proposed DRLSE–based approach to the 3D case [51] for broadband measurements. So far, a multi–frequency analysis can be carried on by performing the DRLSE at each frequency, as depicted in Fig.6. A 3D–DRLSE, instead, would speed up the procedure enabling an automatic and complete 3D dispersion characterization. Finally, to deal simultaneously with multiple modes, the DRLSE will be adapted for the identification of multiple concentric shapes.

ACKNOWLEDGMENT

The research was partially funded by the Polish National Science Center under grant agreement no 2018/29/B/ST8/00045.

REFERENCES

[1] Z. Su, L. Ye, and Y. Lu, "Guided lamb waves for identification of damage in composite structures: A review," *Journal of sound and vibration*, vol. 295, no. 3-5, pp. 753–780, 2006.

[2] B. Hosten and M. Castaings, "Finite elements methods for modeling the guided waves propagation in structures with weak interfaces," *The Journal of the Acoustical Society of America*, vol. 117, no. 3, pp. 1108–1113, 2005.

[3] T. Hayashi and D. Inoue, "Calculation of leaky lamb waves with a semi-analytical finite element method," *Ultrasonics*, vol. 54, no. 6, pp. 1460–1469, 2014.

[4] P. Bocchini, A. Marzani, and E. Viola, "Graphical user interface for guided acoustic waves," *Journal of Computing in Civil Engineering*, vol. 25, no. 3, pp. 202–210, 2011.

[5] J. Li, Z. S. Khodaei, and M. Aliabadi, "Boundary element modelling of ultrasonic lamb waves for structural health monitoring," *Smart Materials and Structures*, vol. 29, no. 10, p. 105030, 2020.

[6] Y. Cho and J. L. Rose, "A boundary element solution for a mode conversion study on the edge reflection of lamb waves," *The Journal of the Acoustical Society of America*, vol. 99, no. 4, pp. 2097–2109, 1996.

[7] P. Kudela, A. Żak, M. Krawczuk, and W. Ostachowicz, "Modelling of wave propagation in composite plates using the time domain spectral element method," *Journal of Sound and Vibration*, vol. 302, no. 4-5, pp. 728–745, 2007.

[8] A. Kamal and V. Giurgiutiu, "Stiffness transfer matrix method (stmm) for stable dispersion curves solution in anisotropic composites," in *Health Monitoring of Structural and Biological Systems 2014*, vol. 9064. International Society for Optics and Photonics, 2014, p. 906410.

[9] B. Pavlakovic, M. Lowe, D. Alleyne, and P. Cawley, "Disperse: A general purpose program for creating dispersion curves," in *Review of progress in quantitative nondestructive evaluation*. Springer, 1997, pp. 185–192.

[10] P. Kudela, M. Radzienski, P. Fiborek, and T. Wandowski, "Elastic constants identification of woven fabric reinforced composites by using guided wave dispersion curves and genetic algorithm," *Composite Structures*, p. 112569, 2020.

[11] M. M. Malatesta, D. Bogomolov, M. Messina, D. D'Ippolito, N. Testoni, L. De Marchi, and A. Marzani, "The delay multiply and sum algorithm for lamb waves based structural health monitoring," in *European Workshop on Structural Health Monitoring*. Springer, 2020, pp. 657–666.

[12] K. Xu, D. Ta, P. Moilanen, and W. Wang, "Mode separation of lamb waves based on dispersion compensation method," *The Journal of the Acoustical Society of America*, vol. 131, no. 4, pp. 2714–2722, 2012.

[13] Z. Sharif-Khodaei and M. Aliabadi, "Assessment of delay-and-sum algorithms for damage detection in aluminium and composite plates," *Smart materials and structures*, vol. 23, no. 7, p. 075007, 2014.

[14] C. Chang and F. Yuan, "Dispersion curve extraction of lamb waves in metallic plates by matrix pencil method," in *Sensors and Smart Structures Technologies for Civil, Mechanical, and Aerospace Systems 2017*, vol. 10168. International Society for Optics and Photonics, 2017, p. 1016807.

[15] F. Schöpfer, F. Binder, A. Wöstehoff, T. Schuster, S. von Ende, S. Föll, and R. Lammering, "Accurate determination of dispersion curves of guided waves in plates by applying the matrix pencil method to laser vibrometer measurement data," *CEAS Aeronautical Journal*, vol. 4, no. 1, pp. 61–68, 2013.

[16] M. Harb and F. Yuan, "A rapid, fully non-contact, hybrid system for generating lamb wave dispersion curves," *Ultrasonics*, vol. 61, pp. 62–70, 2015.

[17] B. Hernandez Crespo, C. R. Courtney, and B. Engineer, "Calculation of guided wave dispersion characteristics using a three-transducer measurement system," *Applied Sciences*, vol. 8, no. 8, p. 1253, 2018.

[18] L. Zeng, L. Huang, X. Cao, and F. Gao, "Determination of lamb wave phase velocity dispersion using time–frequency analysis," *Smart Materials and Structures*, vol. 28, no. 11, p. 115029, 2019.

[19] K. Xu, J.-G. Minonzio, D. Ta, B. Hu, W. Wang, and P. Laugier, "Sparse svd method for high-resolution extraction of the dispersion curves of ultrasonic guided waves," *IEEE transactions on ultrasonics, ferroelectrics, and frequency control*, vol. 63, no. 10, pp. 1514–1524, 2016.

[20] P. Zabbal, G. Ribay, B. Chapuis, and J. Jumel, "Multichannel multiple signal classification for dispersion curves extraction of ultrasonic guided waves," *The Journal of the Acoustical Society of America*, vol. 143, no. 2, pp. EL87–EL92, 2018.

[21] Z. Tian and L. Yu, "Lamb wave frequency–wavenumber analysis and decomposition," *Journal of Intelligent Material Systems and Structures*, vol. 25, no. 9, pp. 1107–1123, 2014.

[22] K. Xu, D. Ta, and W. Wang, "Multiridge-based analysis for separating individual modes from multimodal guided wave signals in long bones," *IEEE transactions on ultrasonics, ferroelectrics, and frequency control*, vol. 57, no. 11, pp. 2480–2490, 2010.

[23] S. Sabeti, C. A. Leckey, L. De Marchi, and J. B. Harley, "Sparse wavenumber recovery and prediction of anisotropic guided waves in composites: A comparative study," *IEEE transactions on ultrasonics, ferroelectrics, and frequency control*, vol. 66, no. 8, pp. 1352–1363, 2019.

[24] C. Li, C. Xu, C. Gui, and M. D. Fox, "Distance regularized level set evolution and its application to image segmentation," *IEEE transactions on image processing*, vol. 19, no. 12, pp. 3243–3254, 2010.

[25] K. B. Prakash, S. Zhou, T. C. Morgan, D. F. Hanley, and W. L. Nowinski, "Segmentation and quantification of intra-ventricular/cerebral hemorrhage in ct scans by modified distance regularized level set evolution technique," *International journal of computer assisted radiology and surgery*, vol. 7, no. 5, pp. 785–798, 2012.

[26] Y. Chen, G. Chen, Y. Wang, N. Dey, R. S. Sherratt, and F. Shi, "A distance regularized level-set evolution model based mri dataset segmentation of brain's caudate nucleus," *IEEE Access*, vol. 7, pp. 124 128–124 140, 2019.

[27] S. Nanthakumar, T. Lahmer, X. Zhuang, G. Zi, and T. Rabczuk, "Detection of material interfaces using a regularized level set method in

piezoelectric structures," *Inverse Problems in Science and Engineering*, vol. 24, no. 1, pp. 153–176, 2016.
[28] A. M. Braga, R. C. Marques, F. A. Rodrigues, and F. N. Medeiros, "A median regularized level set for hierarchical segmentation of sar images," *IEEE Geoscience and Remote Sensing Letters*, vol. 14, no. 7, pp. 1171–1175, 2017.
[29] Ł. Pieczonka, Ł. Ambroziński, W. J. Staszewski, D. Barnoncel, and P. Pérès, "Damage detection in composite panels based on mode-converted lamb waves sensed using 3d laser scanning vibrometer," *Optics and lasers in engineering*, vol. 99, pp. 80–87, 2017.
[30] D. Alleyne and P. Cawley, "A two-dimensional fourier transform method for the measurement of propagating multimode signals," *The Journal of the Acoustical Society of America*, vol. 89, no. 3, pp. 1159–1168, 1991.
[31] M. Ruzzene, "Frequency-wavenumber domain filtering for improved damage visualization," in *Ultrasonic and Advanced Methods for Non-destructive Testing and Material Characterization*. World Scientific, 2007, pp. 591–611.
[32] P. Kudela, M. Radzieński, and W. Ostachowicz, "Identification of cracks in thin-walled structures by means of wavenumber filtering," *Mechanical Systems and Signal Processing*, vol. 50, pp. 456–466, 2015.
[33] H. Sohn, D. Dutta, J. Yang, M. DeSimio, S. Olson, and E. Swenson, "Automated detection of delamination and disbond from wavefield images obtained using a scanning laser vibrometer," *Smart Materials and Structures*, vol. 20, no. 4, p. 045017, 2011.
[34] G. Sha, M. Radzienski, R. Soman, T. Wandowski, M. Cao, and W. Ostachowicz, "Delamination imaging in laminated composite plates using 2d wavelet analysis of guided wavefields," *Smart Materials and Structures*, vol. 30, no. 1, p. 015001, 2020.
[35] L. De Marchi, E. Baravelli, M. Ruzzene, N. Speciale, and G. Masetti, "Guided wave expansion in warped curvelet frames," *IEEE transactions on ultrasonics, ferroelectrics, and frequency control*, vol. 59, no. 5, pp. 949–957, 2012.
[36] L. Yu and Z. Tian, "Lamb wave structural health monitoring using a hybrid pzt-laser vibrometer approach," *Structural Health Monitoring*, vol. 12, no. 5-6, pp. 469–483, 2013.
[37] F. Cabello, J. León, Y. Iano, and R. Arthur, "Implementation of a fixed-point 2d gaussian filter for image processing based on fpga," in *2015 Signal Processing: Algorithms, Architectures, Arrangements, and Applications (SPA)*. IEEE, 2015, pp. 28–33.
[38] Z. Ma and L. Yu, "Lamb wave imaging with actuator network for damage quantification in aluminum plate structures," *Journal of Intelligent Material Systems and Structures*, vol. 32, no. 2, pp. 182–195, 2021.
[39] G. Aubert and P. Kornprobst, *Mathematical problems in image processing: partial differential equations and the calculus of variations*. Springer Science & Business Media, 2006, vol. 147.
[40] S. Qaisar, R. M. Bilal, W. Iqbal, M. Naureen, and S. Lee, "Compressive sensing: From theory to applications, a survey," *Journal of Communications and networks*, vol. 15, no. 5, pp. 443–456, 2013.
[41] Y. K. Esfandabadi, L. De Marchi, N. Testoni, A. Marzani, and G. Masetti, "Full wavefield analysis and damage imaging through compressive sensing in lamb wave inspections," *IEEE transactions on ultrasonics, ferroelectrics, and frequency control*, vol. 65, no. 2, pp. 269–280, 2017.
[42] Y. Keshmiri Esfandabadi, M. Bilodeau, P. Masson, and L. De Marchi, "Deep learning for enhancing wavefield image quality in fast non-contact inspections," *Structural Health Monitoring*, vol. 19, no. 4, pp. 1003–1016, 2020.
[43] J. B. Harley and J. M. Moura, "Sparse recovery of the multimodal and dispersive characteristics of lamb waves," *The Journal of the Acoustical Society of America*, vol. 133, no. 5, pp. 2732–2745, 2013.
[44] J. A. Tropp and A. C. Gilbert, "Signal recovery from random measurements via orthogonal matching pursuit," *IEEE Transactions on information theory*, vol. 53, no. 12, pp. 4655–4666, 2007.
[45] S. Sabeti and J. B. Harley, "Two-dimensional sparse wavenumber recovery for guided wavefields," in *AIP Conference Proceedings*, vol. 1949, no. 1. AIP Publishing LLC, 2018, p. 230003.
[46] Y. Fang, J. Wu, and B. Huang, "2d sparse signal recovery via 2d orthogonal matching pursuit," *Science China Information Sciences*, vol. 55, no. 4, pp. 889–897, 2012.
[47] J. Moll, J. Kathol, C.-P. Fritzen, M. Moix-Bonet, M. Rennoch, M. Koerdt, A. S. Herrmann, M. G. Sause, and M. Bach, "Open guided waves: online platform for ultrasonic guided wave measurements," *Structural Health Monitoring*, vol. 18, no. 5-6, pp. 1903–1914, 2019.
[48] P. Kudela, M. Radzienski, P. Fiborek, and T. Wandowski, "Elastic constants identification of fibre-reinforced composites by using guided wave dispersion curves and genetic algorithm for improved simulations," *Composite Structures*, vol. 272, p. 114178, 2021.
[49] M. Golub, J. Moll, T. Ebert, E. Glushkov, N. Glushkova, C. Fritzen, and O. Nelles, "Experimentally based modeling of non-axisymmetric lamb wave propagation from circular pzts," in *ECCOMAS Thematic Conference on Smart Structures and Materials*, 2011, pp. 486–492.
[50] L. Wang and F. Yuan, "Group velocity and characteristic wave curves of lamb waves in composites: Modeling and experiments," *Composites science and technology*, vol. 67, no. 7-8, pp. 1370–1384, 2007.
[51] C. R. Ng, J. C. M. Than, O. M. Rijal, R. M. Kassim, A. Yunus, and N. M. Noor, "Construction of 3d lung image morphology using 3d distance regularized level set," *ARPN Journal of Engineering and Applied Sciences*, vol. 14, no. 1, pp. 109–113, 2019.

Michelangelo Maria Malatesta (Student Member, IEEE) received the M.S. degree in electronic engineering from the University of Bologna, Italy, in 2018, where he is currently pursuing the Ph.D. degree in Structural and Environmental Health Monitoring and Management. His research interests include signal processing for guided waves inspection, sensors development for SHM and NDE methods.

Jochen Moll received the Dipl.Ing. and Ph.D. degrees in mechanical engineering from the University of Siegen, Germany, in 2007 and 2011, respectively. Presently, he is a Postdoctoral Research Assistant with Goethe University Frankfurt, Germany. His research interests include ultrasonic guided waves, signal processing and imaging techniques. His research profile is located on http://www.jochenmoll.de.

Pawel Kudela received a PhD and habilitation degrees in mechanical engineering from the Institute of Fluid-Flow Machinery, Polish Academy of Sciences in 2009 and 2016, respectively. Currently, he is an associate professor at the same Institute. The common denominator of his scientific interests is guided-wave based structural health monitoring and non-destructive testing. It includes aspects such as modelling elastic waves by using the spectral element method, signal processing, metamaterials and most recently deep learning.

Maciej Radzieński received his Master's degree in electric engineering from Gdynia Maritime University in 2007, Ph.D. degree in control engineering and robotics from Gdańsk University of Technology in 2015, and D.Sc. degree in mechanical engineering from the Institute of Fluid-Flow Machinery in 2020, where he is currently working as research associate. His scientific interests are focused on signal processing in the application of elastic waves for structural health monitoring and non-destructive testing.

Luca De Marchi (Member, IEEE) is currently an Associate Professor in electronics at the University of Bologna, Italy. He has published more than 140 articles in international journals or in proceedings of international conferences. He holds two patents. His current research interests are in multiresolution and adaptive signal processing, with a particular emphasis on SHM applications.